

Breaking Scaling Relations for Highly Efficient Electroreduction of CO₂ to CO on Atomically Dispersed Heteronuclear Dual-Atom Catalyst

Song Lu, Michal Mazur,* Kun Guo, Dragos Constantin Stoian, Minfen Gu, Wakshum Mekonnen Tucho, and Zhixin Yu*

Conversion of CO₂ into value-added products by electrocatalysis provides a promising way to mitigate energy and environmental problems. However, it is greatly limited by the scaling relationship between the adsorption strength of intermediates. Herein, Mn and Ni single-atom catalysts, homonuclear dual-atom catalysts (DACs), and heteronuclear DACs are synthesized. Aberration-corrected annular dark-field scanning transmission electron microscopy (ADF-STEM) and X-ray absorption spectroscopy characterization uncovered the existence of the Mn–Ni pair in Mn–Ni DAC. X-ray photoelectron spectroscopy and X-ray absorption near-edge spectroscopy reveal that Mn donated electrons to Ni atoms in Mn–Ni DAC. Consequently, Mn–Ni DAC displays the highest CO Faradaic efficiency of 98.7% at –0.7 V versus reversible hydrogen electrode (vs RHE) with CO partial current density of 16.8 mA cm^{–2}. Density functional theory calculations disclose that the scaling relationship between the binding strength of intermediates is broken, resulting in superior performance for ECR to CO over Mn–Ni–NC catalyst.

neutrality and sustainable development.^[1–3] Among possible reaction pathways, ECR to CO through two proton–electron pairs transfer is one of the most practical targets due to high selectivity and mild reaction condition.^[4,5] Moreover, CO is a key feedstock for a number of industrial processes to produce various fuels and chemicals.^[6,7] Despite substantial efforts, this process is still limited by a high energy barrier for CO₂ activation, sluggish reaction kinetics, and inevitable competitive hydrogen evolution reaction (HER).^[8–10]

In the past decade, there has been widespread research on single-atom catalysts (SACs) for electrocatalysis, owing to their high atom-utilization efficiency, unique electronic properties, and well-defined active sites.^[11–16] Especially, atomically dispersed transition metals embedded in nitrogen-doped carbon (TM–N–C) have demonstrated good activity for ECR to

CO.^[17–19] However, the single active center makes it difficult to break the constraint of scaling relationship between the adsorption energies of intermediates due to the complicated multiple proton-coupled electron transfer. The overall reaction process for

1. Introduction

Electrochemical CO₂ reduction reaction (ECR) driven by green electricity is one of the most promising ways to achieve carbon

S. Lu, Z. Yu
Department of Energy and Petroleum Engineering
University of Stavanger
Stavanger 4036, Norway
E-mail: zhixin.yu@uis.no

M. Mazur
Department of Physical and Macromolecular Chemistry
Faculty of Science
Charles University
Prague 2 12843, Czech Republic
E-mail: michal.mazur@natur.cuni.cz

K. Guo
School of Materials Science and Engineering
Huazhong University of Science and Technology
Wuhan 430074, China

D. C. Stoian
Swiss-Norwegian Beamlines
European Synchrotron Radiation Facility
Cedex 9, Grenoble 38043, France

M. Gu
Center for Analysis and Testing
Nanjing Normal University
Nanjing 210023, China

W. M. Tucho
Department of Mechanical and Structural Engineering and Material Science
University of Stavanger
Stavanger 4036, Norway

 The ORCID identification number(s) for the author(s) of this article can be found under <https://doi.org/10.1002/smll.202309251>

© 2023 The Authors. Small published by Wiley-VCH GmbH. This is an open access article under the terms of the Creative Commons Attribution License, which permits use, distribution and reproduction in any medium, provided the original work is properly cited.

DOI: 10.1002/smll.202309251

CO generation includes I) $\text{CO}_2 + (\text{H}^+ + \text{e}^-) \rightarrow \text{*COOH}$, II) $\text{*COOH} + (\text{H}^+ + \text{e}^-) \rightarrow \text{*CO} + \text{H}_2\text{O}$, and III) $\text{CO*} \rightarrow \text{CO} + \text{*}$.^[20,21] It has been reported that Ni and Cu SACs generally exhibit excellent CO desorption properties and suppress HER but suffer from the slow *COOH formation step.^[22,23] In contrast, Fe and Co SACs have a low energy barrier for the first proton-coupled electron transfer step, but *CO desorption can be difficult due to the strong affinity of CO to Fe and Co.^[24,25] Therefore, the performance of ECR to CO on these SACs is restricted by the binding of *COOH and *CO that are either too weak or too strong. It is well known that the geometric and electronic structures of the active sites are closely correlated with the catalytic performance.^[26–29] Thus, regulating the structural and electronic properties of the SAC active center is a potential strategy to tune the binding strength between the reaction intermediates and the metal active center to achieve high ECR to CO activity.

Constructing heteronuclear dimer sites to form dual-atom catalysts (DACs) is an efficient way to modify the coordination environment and the electronic properties of the SAC active centers. For instance, heteronuclear DACs such as Fe–Ni, Ni–Cu, Zn–Ni, and Co–Cu DACs anchored on nitrogenated carbon exhibited superior activity for ECR to CO due to the lower energy barrier for the formation of *COOH and desorption of *CO .^[30–33] In another study, Mn–Ni dual-atoms have been reported to modify the electronic structure of Ni active center, which could tune the binding strength of intermediates and facilitate oxygen evolution reaction (OER).^[34] Very recently, ECR to CO was attempted on homonuclear DACs, including Ni–Ni and Mn–Mn, Pd–Pd, and Zn–Zn, among which Ni–Ni exhibited Faradaic efficiency for CO generation (FE_{CO}) of 99%.^[35] In situ characterization combined with theoretical calculation revealed that Ni dual-atom sites could promote *OH adsorption, which triggered electron accumulation at the active centers. As a result, the kinetic barriers of *COOH and *CO desorption were reduced.

Among 3d transition metal-based SACs, Mn SACs displayed weak *CO desorption capability, resulting in low activity for ECR to CO.^[36] Meanwhile, the Mn–Ni DAC has demonstrated great performance in OER because of Mn tuning the electron structure of Ni atom.^[34] Therefore, it is intriguing to explore the structural transformation from SAC to DAC during ECR and the function of the dual atom pairs. This could be achieved by performing a systematic study on SACs, homonuclear DACs, and heteronuclear DACs for a specific catalyst system, and the transition of the active sites.

In this work, Ni SAC (Ni–NC), Mn SAC (Mn–NC), Ni–Ni DAC (Ni–Ni–NC), Mn–Mn DAC (Mn–Mn–NC), and Mn–Ni DAC (Mn–Ni–NC) were synthesized by a facile method. The catalyst with Mn–Ni atom pair exhibited outstanding catalytic activity and selectivity, achieving a maximum FE_{CO} of 98.7% at the potential of -0.7 V (vs RHE) with a CO partial current density of 16.8 mA cm^{-2} , outperforming the homonuclear Ni–Ni DACs and Ni SACs. It also shows excellent stability in the long-time durability test. Aberration-corrected annular dark-field scanning transmission electron microscopy (ADF-STEM) demonstrated the presence of dual-atom pairs in the DACs. Extended X-ray absorption fine structure (EXAFS) characterization uncovered that nonbridged (metal–metal) N_6 is the most possible coordination in DACs. X-ray photoelectron spectroscopy (XPS) and X-ray absorption near-edge spectroscopy (XANES) confirmed electron trans-

fer from Mn to Ni atom in Mn–Ni DAC. Density functional theory (DFT) calculations uncovered the structural evolution of active sites for different intermediates, in which Mn atom could selectively bond with intermediates during the ECR to CO. Mn and Ni atoms work synergistically for *COOH formation, which is not possible for the SACs. Then Ni atom works as the sole adsorption site for *CO adsorption, which is not observed for the Mn–Mn and Ni–Ni homonuclear DACs. Therefore, for the first time, we disclosed that the highly efficient ECR to CO on heteronuclear DACs is attributed to the electron interaction of Mn–Ni atom pair, which could break the scaling relationship of adsorption energies of intermediates.

2. Results and Discussion

2.1. Electrocatalysts Characterization

Mn–NC, Ni–NC, Mn–Mn–NC, Ni–Ni–NC, and Mn–Ni–NC catalysts were prepared by facile ion-adsorption and pyrolysis treatment. Homonuclear DACs were synthesized through coprolysis of metal salts and chelating agent complexes adsorbed on carbon carrier mixed with N sources under 800°C . Mn^{2+} and Ni^{2+} were selected as metal precursors. Carbon black was employed as a carbon substrate due to its low cost and excellent conductivity. Citric acid and dicyandiamide acted as chelating agents and N sources. Heteronuclear DACs and SACs were fabricated through a similar procedure but with the addition of an ammonia solution in the first step. The formation mechanism of homonuclear DACs has been reported recently, in which Ni atoms were captured by the double vacancies of the carbon framework during pyrolysis.^[35]

The crystal structures of the five catalysts were verified by powder X-ray diffraction (XRD) and Raman spectroscopy analyses. As shown in Figure S1a (Supporting Information), the five catalysts all present the same diffraction patterns. Two characteristic peaks located $\approx 24.9^\circ$ and 43.3° can be assigned to the (002) and (001) planes of graphite with low crystallinity. Besides, no peaks attributable to metal or metallic compounds are identifiable, indicating that the metal atoms are possibly dispersed atomically in the carbon matrix.

Figure S1b (Supporting Information) presents the Raman spectroscopy of the five electrocatalysts, which exhibit two vibrational bands of graphite at $\approx 1343 \text{ cm}^{-1}$ (D band) and 1594 cm^{-1} (G band), corresponding to the defect and graphitic sp^2 -hybridized carbon.^[37,38] The ratios between the D and G bands of the catalysts range from 1.03 to 1.09, suggesting a similar graphitization degree and the presence of defects such as vacancies, edges, and nonhexagonal rings.^[39,40]

The textural properties of the electrocatalysts were investigated by N_2 physisorption analyses. As illustrated in Figure S2 (Supporting Information), the isotherms of the five catalysts exhibited sharp adsorption under relative pressures higher than 0.40 accompanied by an obvious hysteresis loop, which can be attributed to the dominant mesopores and is further confirmed by the pore size distributions. The Brunauer–Emmett–Teller (BET) surface area of Mn–NC, Ni–NC, Mn–Mn–NC, Ni–Ni–NC, and Mn–Ni–NC catalysts are 890, 987, 854, 964, and $935 \text{ m}^2 \text{ g}^{-1}$, respectively (Table S1, Supporting Information). The average pore diameters are also very close at $\approx 4.9 \text{ nm}$, while the pore volumes

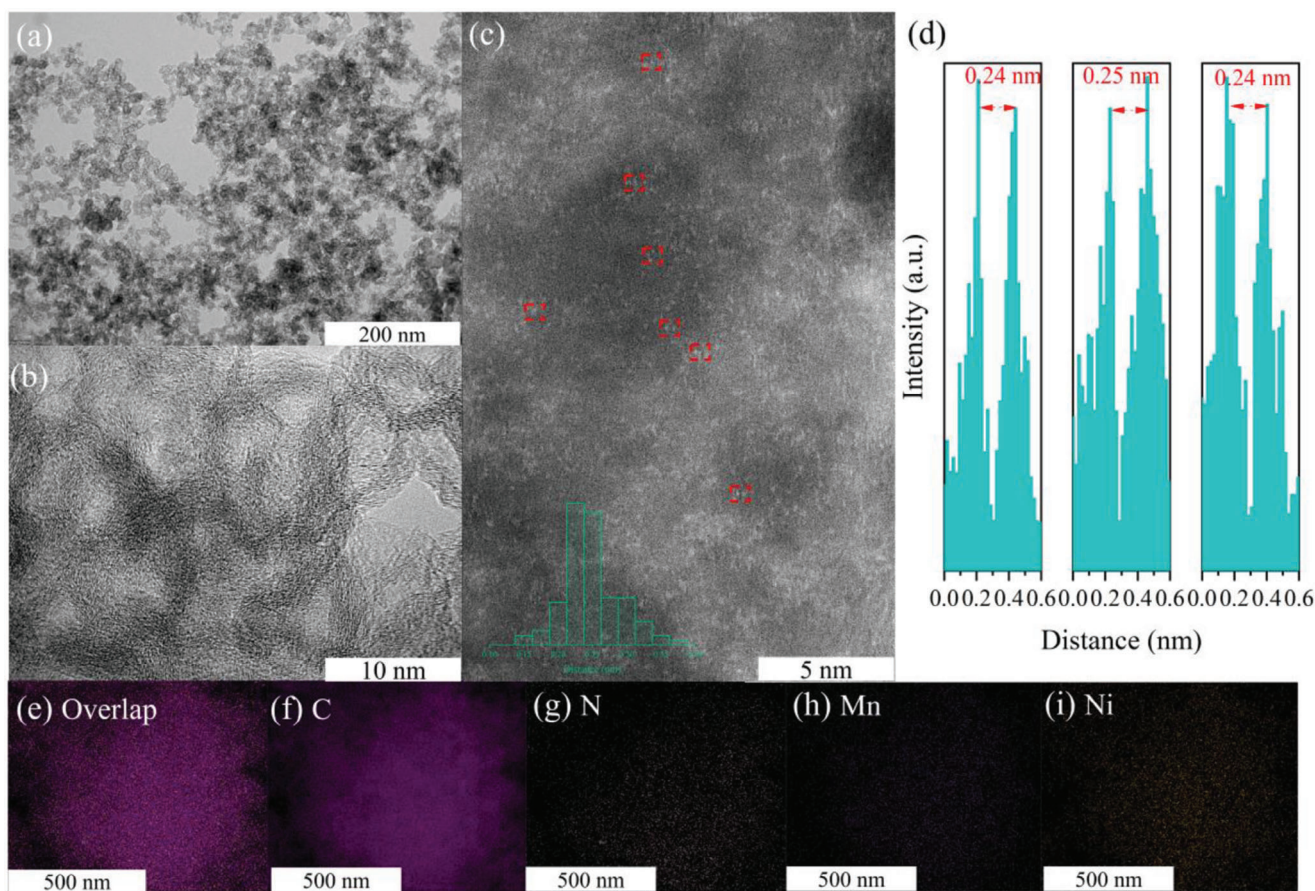


Figure 1. a) TEM, b) HRTEM, and c) ADF-STEM of Mn–Ni–NC, where Mn–Ni atom pair is highlighted in red rectangles, and the histogram shows the proportion of different distances; d) the intensity profile of distance between Mn and Ni atoms; e–i) C, N, Mn, and Ni EDX mapping images of Mn–Ni–NC catalyst.

vary very narrowly from 1.02 to 1.11 cm³ g^{−1}. Therefore, all catalysts exhibit large BET surface area and abundant mesopores, which are beneficial for mass transfer and accessible active sites. It is worth emphasizing that the differences in structure properties of the five catalysts are insignificant, implying that the performance of ECR to CO over the five electrocatalysts can be exclusively ascribed to the intrinsic activities of the catalysts.

TEM characterization shows that the catalysts in general exhibit carbon pellets with a diameter of ≈50 nm (Figure 1a). The high-resolution TEM reveals distorted short-range graphitic stripes with wrinkles and interlaces, suggesting the presence of structural defects in the carbon material (Figure 1b; Figures S4a–S7a, Supporting Information). Besides, no aggregates of metallic nanoparticles could be observed. We further employed ADF-STEM to verify the atomically dispersed metal atoms. As exhibited in Figure 1c and Figures S3a, S4b–S7b (Supporting Information), evenly distributed bright spots could be observed on the carbon framework in the dark field for the Mn–Ni–NC catalyst. These dense bright dots with different brightness could be assigned to metallic Mn and Ni atoms because of the atomic number-dependent contrast difference in the dark field.^[41] Besides, the binding energies of Mn–Ni, Mn–Mn, and Ni–Ni are −11.89, −9.21, and −11.40 eV, respectively. The formation energy of Mn–Ni, Mn–Mn, and Ni–Ni are −10.28, −9.38, and

−10.02 eV, respectively. These results demonstrate that the formation of Mn–Ni pair is preferable. Moreover, numerous neighboring spots marked with red rectangles were observed, indicating that Mn and Ni atoms are present in the form of atom pairs. Statistical analysis was performed for the Mn–Mn–NC, Ni–Ni–NC, and Mn–Ni–NC DAC catalysts. In each sample, 100 dots were fixed and the distance from the closest bright dots was measured. For the Mn–Ni–NC catalyst, 58% dual-atom Mn–Ni pairs were counted, while 42% Mn and Ni atoms were counted as isolated atoms. The distances of the adjacent spots are estimated to be ≈0.24 ± 0.01 nm (Figure 1d). Similarly, 39% Mn–Mn atom pairs were found in Mn–Mn–NC, and 46% Ni–Ni atom pairs were observed for the Ni–Ni–NC catalyst. The distances between the adjacent Mn–Mn and Ni–Ni atoms are both centered at ≈0.23 ± 0.01 nm (Figures S6c and S7c, Supporting Information). Considering the great challenge of identifying each atom by ADF-STEM, this statistic analysis can effectively figure out the distance of neighboring atoms.^[41] In contrast, for the Mn–NC and Ni–NC SAC catalysts, isolated Mn and Ni atoms can be easily observed, even though some Mn–Mn and Ni–Ni atom pairs are also present. Furthermore, energy-dispersive X-ray spectroscopy (EDS) shows that in the Mn–Ni–NC catalyst, C, N, Mn, and Ni elements are homogeneously distributed (Figure 1e–i), which is also apparent for all

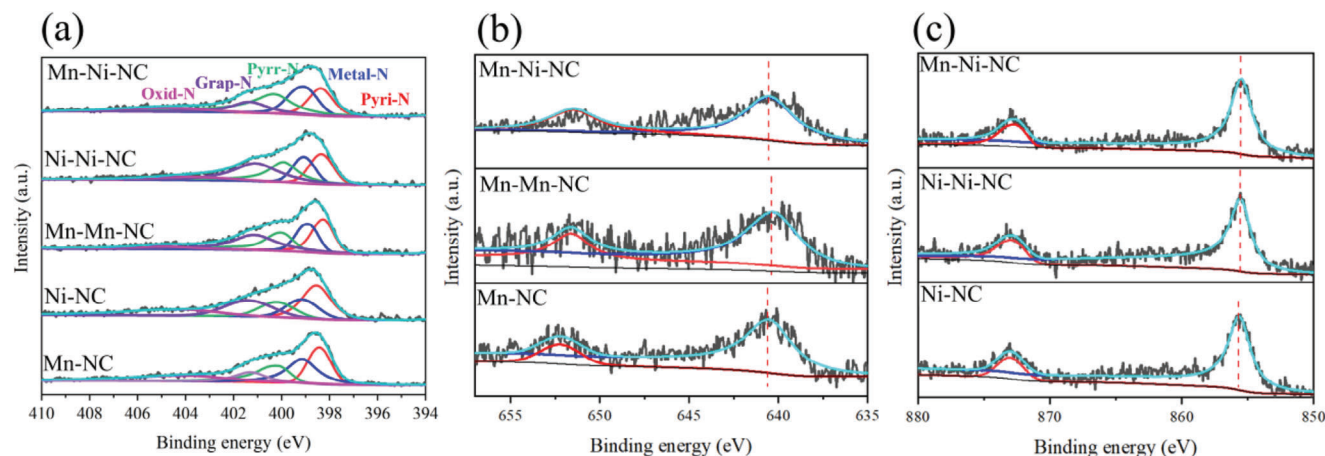


Figure 2. a) High-resolution N 1s XPS spectra of Mn-NC, Ni-NC, Mn-Mn-NC, Ni-Ni-NC and Mn-Ni-NC catalysts; b) high-resolution Mn 2p XPS spectra of Mn-NC, Mn-Mn-NC and Mn-Ni-NC catalysts; c) high-resolution Ni 2p XPS spectra of Ni-NC, Ni-Ni-NC and Mn-Ni-NC catalysts.

other electrocatalysts (Figures S4c–f, S5c–f, S6d–g and S7d–g, Supporting Information). Therefore, it is fair to conclude that Mn-NC and Ni-NC are SACs, while Mn-Mn-NC, Ni-Ni-NC, and Mn-Ni-NC are DACs.

X-ray photoelectron spectroscopy (XPS) was carried out to investigate the chemical species and element states of Mn, Ni, N, and C in the electrocatalysts. As displayed in Figure 2a, the high-resolution N 1s spectra can be deconvoluted into five species: pyridinic (Pyri-N), metallic (Metal-N), pyrrolic (Pyr-N), graphitic (Grap-N), and oxidized (Oxid-N), with corresponding binding energy of 398.3, 400.3, 401.4, and 404.5 eV, respectively.^[42–45] Notably, the peak at 399.1 eV can be assigned to a porphyrin-like metal-N coordination structure, which demonstrates that metal atoms are coordinated with N atoms in the carbon framework.^[46,47] In particular, the existence of Pyri-N in carbon substrates plays a significant role in anchoring and stabilizing single metal atoms as well as promoting electrocatalytic activity.^[48] The Pyri-N concentration is the lowest for the Mn-Ni-NC catalyst, while its metal-N concentration is the highest among the five electrocatalysts. On the other hand, the concentrations of Pyr-N, Grap-N, and Oxid-N did not show obvious differences (Table S2, Supporting Information). The results indicate that most Mn and Ni atoms prefer to bond with Pyri-N. Moreover, the binding energy of Pyri-N in DACs shows a slight downshift in comparison with that in SACs, while the binding energies of metal-N of DACs are similar. Therefore, the electronic structures of SACs and DACs are different. High-resolution Mn-2p spectra in Figure 2b show that the Mn-2p_{3/2} peaks of Mn-NC (640.6 eV), Mn-Mn-NC (640.3 eV) and Mn-Ni-NC (640.5 eV) are located between Mn⁰ (638.7 eV) and Mn²⁺ (641.4 eV).^[49] The Ni-2p_{3/2} peaks of Ni-NC (855.7 eV), Ni-Ni-NC (855.6 eV), and Mn-Ni-NC (855.5 eV) are located between Ni⁰ (852.5 eV) and Ni²⁺ (856.0 eV) (Figure 2c).^[50,51] Therefore, Mn and Ni species probably both have an oxidation state between 0 and +2. It is worth noting that the binding energies of Mn-2p_{3/2} in Mn-Mn-NC and Mn-Ni-NC exhibit a negative shift in comparison to the Mn-NC catalyst. Similarly, the binding energies of Ni-2p_{3/2} in Ni-Ni-NC and Mn-Ni-NC also show a negative shift compared with Ni-NC. Consequently, the oxidation states of Mn and Ni atoms decreased when atom pairs were formed in

DACs. Obviously, when the concentration of Metal-N decreases, less electron are donated from metal to coordinated N atoms. In particular, the binding energies of Mn-2p_{3/2} and Ni-2p_{3/2} in Mn-Ni-NC catalyst are more positive and negative than that of Mn-2p_{3/2} in Mn-Mn-NC, and Ni-2p_{3/2} in Ni-Ni-NC, respectively. Consequently, there are apparent electron transfers between Mn and Ni in Mn-Ni-NC, in which the Ni atom with higher electronegativity attracted electrons from the paired Mn atom. Therefore, XPS characterization evidenced that when atom pairs are formed, there are valence changes in the homonuclear DACs and electron transfer in the heteronuclear DAC.

X-ray adsorption spectroscopy (XAS) was conducted to reveal the detailed electronic structure and coordination environment of the metal active centers. Figure 3a and b depict XANES of Mn and Ni atoms of different catalysts, reference Mn and Ni metal foils, and metal phthalocyanine (Mn-Pc and Ni-Pc). In the Mn K-edge XANES spectra, the near-edge absorption energies of Mn-NC, Mn-Mn-NC, and Mn-Ni-NC are located between those of Mn foil and Mn-Pc, confirming that the oxidation states of Mn are between 0 and +2. Besides, the near-edge absorption energies of the Mn atom in Mn-Ni-NC catalyst show a slightly positive shift compared with that of Mn-Mn-NC, indicating that the valence state of the Mn atom increased. Similarly, Ni K-edge XANES spectra of Ni-NC, Ni-Ni-NC, and Mn-Ni-NC are located between those of Ni foil and Ni-Pc, confirming that the valence states of Ni are also between 0 and +2. In comparison with Ni-Ni-NC, the near-edge absorption energies of Ni in Mn-Ni-NC catalyst show a slight negative shift, demonstrating the decrease of the valence state of Ni. Consequently, Mn donated electrons to Ni in the heteronuclear Mn-Ni-NC DAC, in agreement with XPS analysis.

Figure 3c,d displays the Fourier transform (FT) of k³-weighted EXAFS of Mn and Ni K-edge in the R-space. The Mn K-edge spectra show a major peak at ≈1.5 Å, assigned to the Mn-N coordination in the Mn-NC, Mn-Mn-NC, and Mn-Ni-NC catalysts. A dominant peak at ≈1.3 Å for the Ni K-edge spectra of Ni-NC, Ni-Ni-NC, and Mn-Ni-NC catalysts is associated with the Ni-N bonding. The Mn-Mn (2.3 Å) and Ni-Ni (2.1 Å) bonds are characteristic of Mn and Ni foils. However, the metal-metal bonds are absent in the Mn-NC and Ni-NC

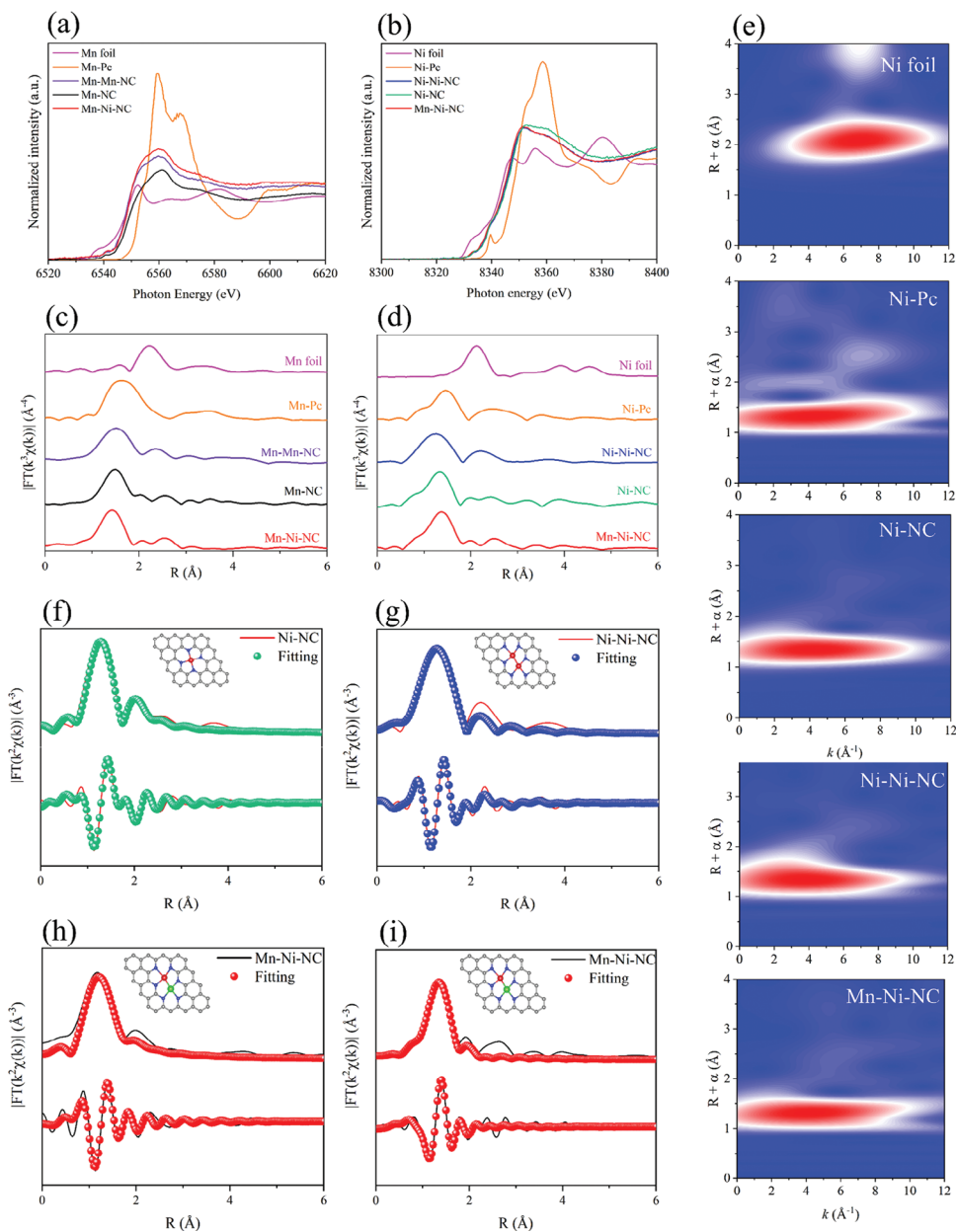


Figure 3. a) Mn K-edge and b) Ni K-edge XANES spectra of the catalysts; c) Mn K-edge and d) Ni K-edge Fourier transform (FT) k^3 -weighted EXAFS (FT-EXAFS) spectra of the samples at R space; e) Ni K-edge Wavelet transformed k^2 -weighted EXAFS plots of Ni foil, Ni-Pc, Ni-NC, Ni-Ni-NC and Mn-Ni-NC; f) Ni-N, g) Ni-N, h) Ni-N and i) Mn-N fittings of the FT-EXAFS spectra for Ni-NC, Ni-Ni-NC, Mn-Ni-NC and Mn-Ni-NC catalysts. The gray, blue, red, and green balls refer to C, N, Ni, and Mn atoms, respectively.

catalysts, which confirms atomically dispersed Ni and Mn atoms. Remarkably, peaks at 2.3 and 2.5 Å in the Mn K-edge spectra can be identified for the Mn-Mn-NC and Mn-Ni-NC catalysts, which can be assigned to Mn-Mn and Mn-Ni coordination, respectively. Similarly, peaks at 2.2 Å and 2.5 Å in the Ni K-edge spectra of Ni-Ni-NC and Mn-Ni-NC catalysts are attributed to Ni-Ni and Mn-Ni coordination. Therefore, the FT-EXAFS analysis demonstrated the formation of atom pairs for all three DACs.

Wavelet transform (WT) EXAFS (WT-EXAFS) oscillations were also conducted to discriminate the backscattering atoms and obtain high resolutions in both K and R spaces. As dis-

played in Figure S8 (Supporting Information), the WT-EXAFS contour plot of Mn foil shows a strong signal with maximum intensity at $\approx 5.1 \text{ \AA}^{-1}$ of the Mn-Mn contributions. However, this signal is absent for the Mn-NC and Mn-Ni-NC catalysts but is slightly visible at $\approx 7.5 \text{ \AA}^{-1}$ for the Mn-Mn-NC catalyst. Similarly, WT-EXAFS of Ni foil shows a prominent feature centered $\approx 7.0 \text{ \AA}^{-1}$, which is not found for the Ni-NC and Mn-Ni-NC catalysts but visible at 6.8 \AA^{-1} for the Ni-Ni-NC catalyst. Similar to the WT-EXAFS contour plots of Mn-Pc, the spectra of Mn-NC, Mn-Mn-NC, Mn-Ni-NC also show strong features at 4.8 \AA^{-1} , which can be attributed to the Mn-N coordination. Meanwhile, a

weak signal at 6.0 \AA^{-1} can be observed for the Mn–Ni–NC catalyst, indicating the Mn–Ni coordination. For the Ni WT-EXAFS contour plots of Ni–NC, Ni–Ni–NC, and Mn–Ni–NC electrocatalysts, a maximum intensity at 4.0 \AA^{-1} due to the Ni–N contribution can be observed (Figure 3e). A weak feature at 6.1 \AA^{-1} is also attributed to the Mn–Ni bonding. It is worth noting that the different models of atomic vibration could cause a difference in signal intensity.^[32] The WT-EXAFS analysis demonstrated that Mn and Ni atoms dispersed atomically on the N-doped carbon substrate, and the existence of Mn–Mn, Ni–Ni, and Mn–Ni bonding for the DACs.

To elaborate the structures of the catalysts, theoretically optimized metal–N configurations based on DFT calculations and fitted-EXAFS curves were constructed. As shown in Figure 3f–i and Figure S9a,b, (Supporting Information) the fitted results in R-space and K-space match well with the experimental spectra. The detailed fitting parameters, e.g., metal–N coordination numbers, and metal–N path length are summarized in Table S3 (Supporting Information). The average metal–N coordination numbers are 4, 4, 3.5, 3.5, and 3.5 for Mn–NC, Ni–NC, Mn–Mn–NC and Ni–Ni–NC and Mn–Ni–NC catalysts, suggesting that Mn and Ni SACs have the usual metal–N₄ center, while the DACs exhibit metal–N₃ configurations. The fitting parameters for Ni–Ni, Mn–Mn, and Mn–Ni interaction paths indicate that the average coordination number of metal–metal is one in the DAC catalysts (Figure S9c–e, Supporting Information). More importantly, the average bond lengths of Mn–Mn, Ni–Ni, and Mn–Ni are 2.40, 2.35, and 2.20 \AA , consistent with ADF-STEM results. Therefore, nonbridged (Mn–Mn)N₆, (Ni–Ni)N₆, and (Mn–Ni)N₆ embedded carbon frameworks were successfully synthesized for DACs, as evidenced by the combination of EXAFS spectra, fitted curves, and DFT calculations.

2.2. Electrocatalytic Activity Test

The ECR performance of the samples was evaluated in a custom-made H-cell with three electrodes system and CO₂-saturated 0.5 M KHCO₃ electrolyte by linear sweep voltammetry (LSV) method. As illustrated in Figure 4a, the Mn–Ni–NC electrocatalyst exhibits the largest current density at all applied potentials. It also exhibits an enhanced current response and a lower onset potential under CO₂ atmosphere than under Ar (Figure 4b), indicating the occurrence of ECR. The potentiostatic electrolysis was conducted under different potentials from -0.3 to -1.0 V versus reversible hydrogen electrode (vs RHE). The gaseous and liquid products were detected by online gas chromatography (GC) and ¹H nuclear magnetic resonance (NMR). As displayed in Figure 4c, ECR to CO on Mn–Ni–NC, Ni–Ni–NC, Ni–NC catalysts occurred under -0.4 V (vs RHE), showing the lower onset potential for ECR to CO. With the increase of the applied potential, the Mn–Ni–NC catalyst reaches the maximum FE_{CO} of 98.7% at the potential of -0.7 V (vs RHE). Besides, FE_{CO} is higher than 90% between -0.5 and -0.9 V (vs RHE), exhibiting wide potential windows. The Ni–Ni–NC and Ni–NC catalysts present the highest FE_{CO} of 91.6% and 87.8% at the potential of -0.8 V (vs RHE).

The Ni–Ni–NC shows slower decay of FE_{CO} than the Ni–NC catalyst with the increase of potential, also implying a wide po-

tential window for highly efficient ECR to CO. It has been reported that the formation of *COOH on the Ni site is difficult due to a large energy barrier.^[52,53] Therefore, the enhanced ECR performance on Ni–Ni–NC could be attributed to the decrease of the energy barrier for the formation of *COOH on Ni–Ni dual sites. The Mn–Mn–NC and Mn–NC catalysts exhibit low FE_{CO} at all applied potentials. Even though forming Mn–Mn atom pairs also improved the ECR performance of Mn–NC, the FE_{CO} of Mn–Mn–NC is still less than 40%. This can be explained by the strong adsorption of *CO on the Mn site. The improvement of ECR performance on Mn–Mn–NC demonstrates that the Mn–Mn site may moderate *CO adsorption to some certain extent. Nevertheless, the competing hydrogen evolution reaction on Mn and Mn–Mn–NC catalysts is dominating, as shown in Figure 4d. Remarkably, the ECR performance to CO on Mn–Ni DAC is greatly improved compared to the Mn and Ni SACs, implying that forming heteronuclear atom pairs could facilitate either *COOH formation or *CO desorption. This could be further ascribed to the moderate binding energies for intermediates due to the electron interaction between the heteronuclear atoms. For the Mn–Ni–NC catalysts, only CO and H₂ products were identified as the products at all applied potentials, with a total FE_{CO} of $\approx 100\%$. No liquid products were detected, as evidenced by ¹H NMR (Figure S10, Supporting Information).

The CO partial current densities on the five catalysts were also calculated (Figure 4e). For the Mn–Ni–NC catalyst, it increased with the applied potential, reaching 16.8 mA cm^{-2} at -0.7 V (vs RHE), which is 1.31, 1.62, 21.3, and 42.2 times higher than that of Ni–Ni–NC, Ni–NC, Mn–Mn–NC, and Mn–NC catalysts. The turnover frequency (TOF) of the five catalysts was calculated to uncover the intrinsic activity of the active site.^[33] As illustrated in Figure 4f, the TOF on the Mn–Ni–NC catalyst is the highest at 2859 h^{-1} at -0.7 V (vs RHE), indicating its high intrinsic activity.

Electrochemical active surface areas (ECSA) play a significant role in ECR activity, which is calculated by measuring double layer (D-L) capacitance (Figure 4g; Figure S11, Supporting Information). The Mn–Ni–NC catalyst has a capacitance of 53.3 mF cm^{-2} , slightly higher than the other catalysts. As a result, the ECSA for Mn–Ni–NC, Ni–Ni–NC, Ni–NC, Mn–Mn–NC, and Mn–NC catalysts were 1332, 1195, 1120, and $980, 927 \text{ cm}^2_{\text{ECSA}}$, demonstrating that the Mn–Ni atoms pair could increase the ESCA. Furthermore, the Tafel slopes on the five samples were compared to disclose the kinetics for CO generation (Figure 4h). An improved Tafel slope of 168 mV dec^{-1} for CO generation on the Mn–Ni–NC catalyst is obtained, attributed to the synergistic effect of the Mn–Ni pair. Additionally, the small Tafel slope also indicates that the rate-limiting step of ECR to CO on the Mn–Ni–NC catalyst is the first protonation of CO₂.^[54,55] Overall, the DAC catalysts show a lower Tafel slope than their SAC counterparts. Dual atom pairs especially with heteronuclear atoms could effectively reduce the Tafel slope, which contributes to a more kinetically favorable ECR to CO. Electrochemical impedance spectroscopy (EIS) indicated that Mn–Ni–NC catalyst has the smallest charge-transfer resistance among the five catalysts (Figure S12, Supporting Information), implying fastest charge transfer. Therefore, the heteroatomic pairs could act synergistically, which outperforms homoatomic pairs and SACs in ECR to CO.

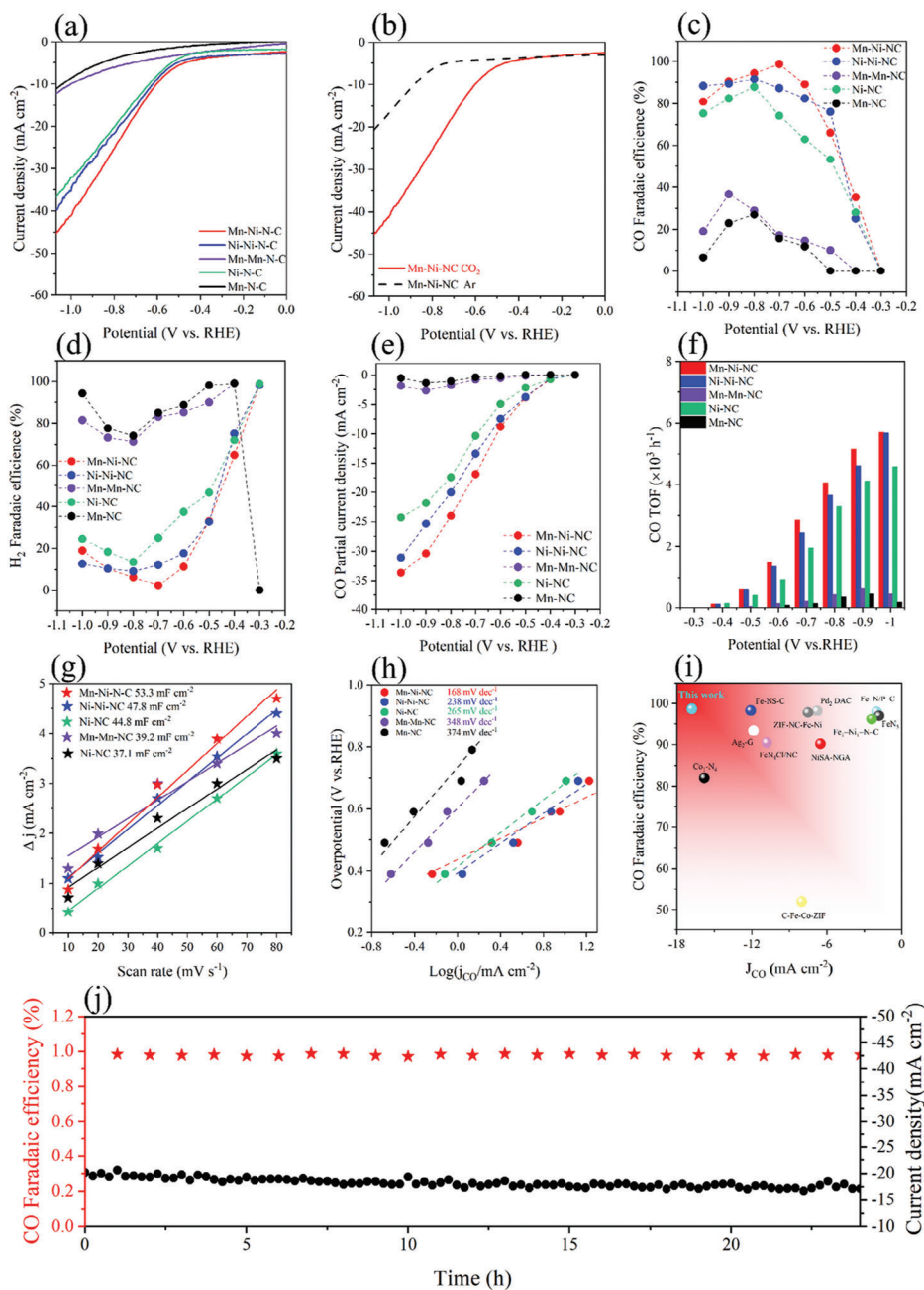


Figure 4. ECR to CO activity of different catalysts. a) LSV curves of the catalysts obtained in CO₂-saturated 0.5 M KHCO₃ electrolyte at the scan rate of 10 mV s⁻¹; b) LSV curves of the Mn–Ni–NC catalyst in Ar- and CO₂-saturated electrolyte; c) Faradaic efficiency for CO; d) Faradaic efficiency for H₂; e) partial current densities of CO and f) TOF for different catalysts at different applied potentials; g) charge current density difference against scan rates of Mn–NC, Ni–NC, Mn–Mn–NC, Ni–Ni–NC, and Mn–Ni–NC catalysts; h) Tafel plots for the CO partial current density; i) comparison of Faradaic efficiency and current density on reported SACs and DACs in H-cell; j) stability test for Mn–Ni–NC at –0.7 V (vs RHE) with 24 h continuous electrocatalytic reaction.

The Mn–Ni–NC catalyst in this study outperformed most of the recently reported SACs and DACs applied for ECR to CO (Figure 4i; Table S4, Supporting Information). Finally, a continuous potentiostatic activity test for 24 h demonstrated that the Mn–Ni–NC catalyst exhibited stable current density and FE_{CO} with negligible decay under the potential of –0.7 V (vs RHE) (Figure 4j).

2.3. DFT Simulation

To uncover the activity origin, DFT calculations were employed based on the EXAFS fitting results. The distribution of electron density on N and coordinated metal atoms of catalysts is correlated with intrinsic activity and ECR selectivity.^[30] After forming Mn–Mn, Ni–Ni, and Mn–Ni atom pairs, the electron

density around the N, Mn, and Ni atoms exhibit apparent changes (Figure S13, Supporting Information). For instance, more electrons accumulate around the metal atoms of the homonuclear atom pair. Charge transfer between Mn and Ni atoms can also be observed, indicating electron interactions after forming atom pairs. Moreover, Bader charge analysis demonstrated that the Mn and Ni atoms always act as electron donors in the single atom center, homonuclear atom pair, and heteronuclear atom pair. The amount of the lost electrons for the Mn atom decreased first and then increased, while it always decreased for Ni atom (Figure 5a). This opposite trend for Mn and Ni atom in the change from homonuclear to heteronuclear pair discloses electron transfer from Mn to Ni atom, which vividly shows the electron interaction between Mn and Ni atoms. Therefore, the valence state of Mn and Ni atoms shows an increase and decrease, consistent with XPS and XANES analysis. Consequently, building dual-atom pairs can regulate the electron density of the active sites in different ways, which directly affects the binding strength of intermediates with active sites.

ECR to CO consists of three steps, i.e., the formation of *COOH, *CO generation, and the desorption of CO. The Gibbs free energy diagrams of each step at $U = 0$ V (vs RHE) were calculated in Figure 5b. As expected, Mn and Ni SACs exhibit a high energy barrier for *COOH production (1.83 eV) or *CO desorption (0.75 eV), resulting from the binding strength between the intermediate and metal sites. After forming a homonuclear atom pair, the energy barrier for *COOH generation on the Ni–Ni–NC catalyst decreased greatly to 0.70 eV. For the Mn–Mn–NC DAC, although the free energy barrier for the formation of *COOH decreased, the desorption of *CO deteriorated remarkably with an energy barrier of 1.88 eV. These changes can be explained by the coordination effect of the dual metal atoms. For the SACs, only one C-metal bond will form for *COOH generation. However, when the dual atom pairs are formed, the C atom of intermediates could bond with two metal atoms with two C-metal bonds. Consequently, the binding strength of intermediates to active sites increased. Notably, as the *COOH formation on the Mn–Mn site is energy favorable, the rate-limiting step will become *CO desorption from the Mn–Mn site, which is controlled by the thermodynamic process. Thus, Mn–Mn sites are potentially passivated by strongly adsorbed *CO, in agreement with other studies.^[21,33] An additional active site could be possible for CO₂ activation on the CO-adsorbed Mn–Mn site (CO*Mn–Mn–NC). The free energy barrier of CO desorption on the site decreased remarkably (0.54 eV), which promotes *CO desorption from the Mn site. The results proved that the ECR performance is improved after incorporating the second homonuclear atom into SACs, in line with experimental observations. For the Mn–Ni–NC catalyst, the energy barrier for *COOH formation on Ni and Mn sites are 0.40 and 0.51 eV, lower than that of Mn, Ni, CO*Mn–Mn, and Ni–Ni catalysts. However, the free energy barrier for *CO desorption from the Ni site is only 0.39 eV, much lower than that of the Mn site (0.85 eV). Although DACs may offer potential active sites for C–C coupling, it is not considered in this study because of difficult kinetics.

As depicted in Figure 5c, the free energy change for *COOH formation and *CO desorption was built to reveal the scaling relationship of intermediates. Unexpectedly, the scaling relationship of the binding strength of intermediates on Mn–Ni DAC was

broken. This can be explained by that C atom of *CO prefer to bond with Ni atom on Ni site, while the C atom of *CO will bond with both Mn and Ni atom on Mn site. In other words, during ECR to CO, the Mn atom can bind the intermediates selectively. For the CO₂ protonation, Mn and Ni atoms act together to accelerate the *COOH formation, which is not possible in Mn and Ni SACs. For the *CO desorption, the Mn atom will not bond with *CO, which promotes CO generation (Figure 5d). However, this cannot be observed in Mn and Ni homonuclear DACs (Figure S14, Supporting Information). Therefore, Mn–Ni–NC catalysts with the lowest energy barriers for both *COOH formation and *CO desorption, due to the synergistic effect of Mn and Ni atoms, which can selectively interact with intermediates. As a result, the restriction of the scaling relationship on the binding strength of intermediates was broken on the Mn–Ni–NC catalyst, resulting in the superior performance of ECR to CO.

As HER is the main competing reaction, the free energy changes of HER on the five catalysts were also calculated. As illustrated in Figure S15a (Supporting Information), Ni–NC shows the largest energy barrier of 1.40 eV for *H generation, while both Ni–Ni–NC and Mn–Ni–NC show an energy barrier of ≈ 0.12 eV. Therefore, an excellent *H generation performance possibly boosts proton transfer, accelerating the ECR to CO process. The selectivity of ECR to CO against HER is evaluated by calculating the difference of limiting potentials between ECR and HER ($U_L(\text{CO}_2) - U_L(\text{H}_2)$), where a more positive value of $U_L(\text{CO}_2) - U_L(\text{H}_2)$ indicates higher ECR selectivity to CO. As depicted in Figure S15b (Supporting Information), Mn–Mn–NC and Ni–Ni–NC show more positive values of $U_L(\text{CO}_2) - U_L(\text{H}_2)$ than their SACs counterparts, confirming that DACs have higher ECR selectivity. Heteronuclear Mn–Ni–NC presents the most positive $U_L(\text{CO}_2) - U_L(\text{H}_2)$ of -0.29 eV, demonstrating its superior ECR selectivity to CO by suppressing HER reaction.

To disclose the effects of electron structure on the adsorption performance of intermediates, the crystal orbital Hamilton population (COHP) and integrated COHP (ICOHP) are employed to further study the interaction strength between the active site and intermediates, in which a positive -COHP indicates bonding state, while a negative -COHP represents the anti-bonding state below Fermi energy. As shown in Figure 5e,f, a more noticeable anti-bonding state appears in CO passivated Mn–Mn–NC catalyst (CO*Mn–Mn–NC) in comparison with Mn–NC, demonstrating weak CO adsorption on the CO*Mn–Mn–NC catalyst. This is also confirmed by the larger ICOHP (-0.48 eV) of CO passivated Mn–Mn–NC catalyst. *COOH cannot adsorb stably on single Ni sites due to the existence of antibonding states (Figure 5g). After introducing the second Ni atom, the antibonding states almost disappeared, implying an improvement in the binding strength between Ni and *COOH (Figure 5h). Despite that the ICOHP of C–Ni over Ni–NC is larger than that of C–Ni over Ni–Ni–NC, C will bond with two Ni atoms, which increases the binding strength compared with a single Ni atom. Finally, we compared the adsorption strength of C and O atoms of *COOH to the Ni and Mn atoms of the Mn–Ni–NC catalyst (Figure 5i,j). Remarkably, both C and O atoms could bind with Ni and Mn atoms strongly, as demonstrated by the absence of antibonding states. Therefore, *COOH generation was enhanced greatly, which endows Mn–Ni–NC with excellent ECR activity. Overall, it can be concluded that the Mn atom donated more electrons in Mn–Ni

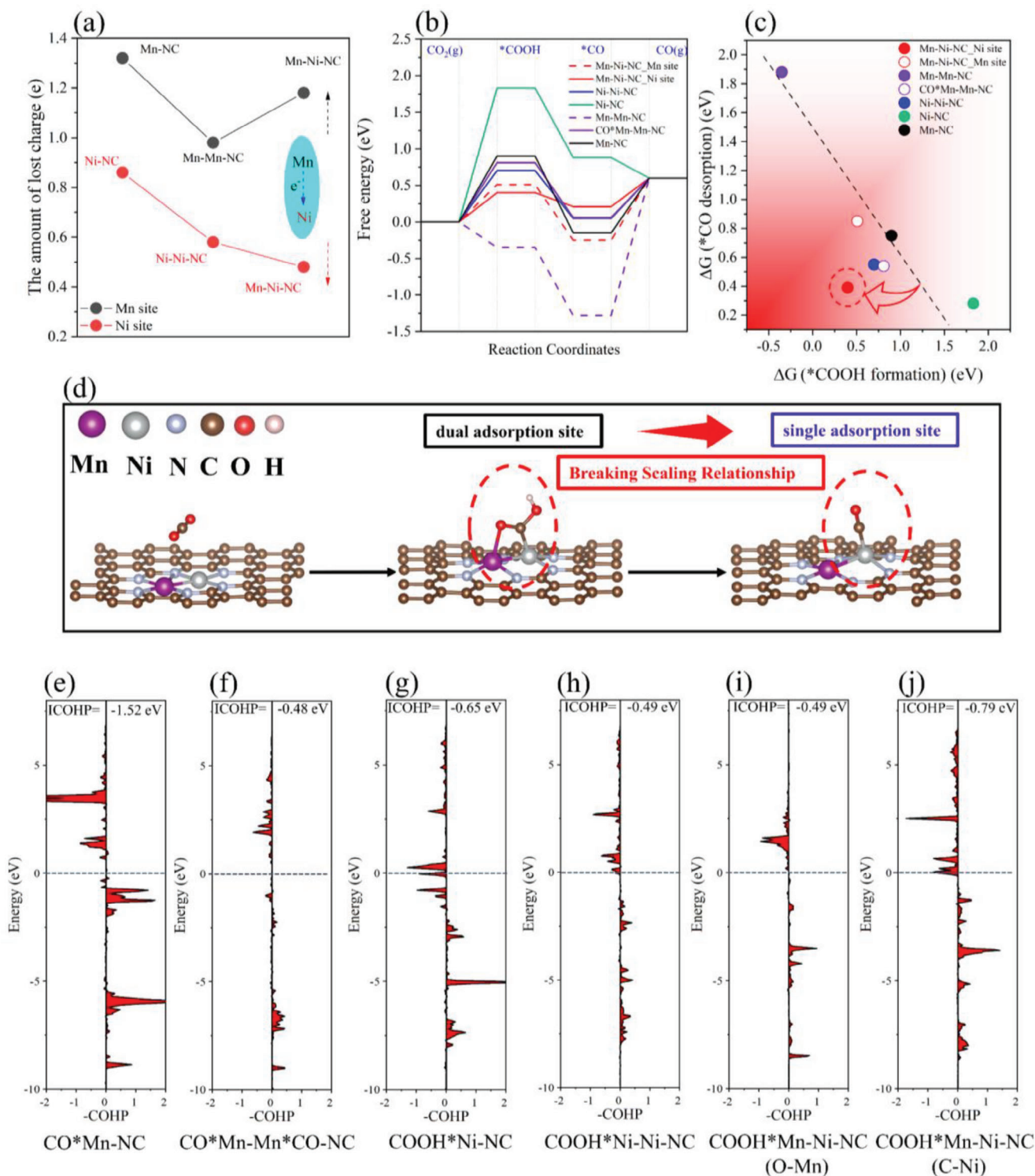


Figure 5. a) Electron transfer between Mn and Ni atoms on different catalysts; b) Gibbs free energy change diagram for ECR to CO on different catalysts; c) scaling relationship between *COOH and *CO; d) the activity mechanism of ECR to CO on Mn–Ni–NC; The COHP distribution of e) CO*Mn–NC, f) the second CO adsorbed on CO passivated Mn–Mn–NC, g) COOH*Ni–NC, h) COOH*Ni–Ni–NC, i) COOH*Mn–Ni–NC (O bonded Mn); j) COOH*Mn–Ni–NC (C bonded Ni), where Fermi level is set to zero.

than the Mn–Mn atom pairs, causing a higher valence state of Mn and stronger *CO binding strength. However, the valence state of Ni atom decreased in Mn–Ni compared with the Ni–Ni center, resulting in superior *COOH binding strength. Consequently, electron interaction between Mn and Ni atoms in the Mn–Ni–NC catalyst resulted in moderate and low valence states for Mn and Ni atoms respectively, which directly influenced the binding strength of the intermediate. Meanwhile, the selective adsorption of intermediates on the active center contributes to breaking the scaling relationship, which greatly improves the performance of ECR to CO.

3. Conclusion

A series of SACs and DACs including Mn–NC, Mn–Mn–NC, Ni–NC, Ni–Ni–NC, and Mn–Ni–NC electrocatalysts were systematically studied for ECR to CO to reveal the evolution of the activity. ADF-STEM and EXAFS characterizations demonstrated the presence of atom pairs in DACs, displaying nonbridged (metal–metal)₆ coordination. Electron transfer from Mn to Ni atom as evidenced for the heteronuclear Mn–Ni–NC catalyst through XPS and XANES. The Mn–Ni–NC catalyst displayed the highest FE_{CO} of 98.7% at the potential of –0.7 V (vs RHE) with CO partial current density of 16.8 mA cm^{–2}, achieving a TOF of 2859 h^{–1}. DFT calculations disclosed that Mn atoms with a high oxidation state resulted in strong CO binding strength, while the low valence state of Ni atom contributed to superior *COOH binding strength, which promotes ECR to CO. More importantly, the *COOH or *CO intermediates could change their binding sites during ECR to CO. The C and O atoms of *COOH prefer to bind with Ni and Mn atoms, respectively, promoting CO₂ protonation. Only Ni atom will bind with C atom of *CO, thus accelerating CO generation. However, the change in binding sites is only observed for heteronuclear DAC, because the heteronuclear metal atom pair could break the scaling relationship of the adsorption strength of intermediates.

Supporting Information

Supporting Information is available from the Wiley Online Library or from the author.

Acknowledgements

This work was supported by the Norwegian Ministry of Education and Research. The computations were performed on resources provided by UNINETT Sigma2 – the National Infrastructure for High Performance Computing and Data Storage in Norway. M.M. would like to acknowledge the Czech Science Foundation for the ExPro project (19–27551X) and OP VVV “Excellent Research Teams,” project No. CZ.02.1.01/0.0/0.0/15_003/0000417–CUCAM.

Conflict of Interest

The authors declare no conflict of interest.

Author Contributions

The manuscript was written through the contributions of all authors. All authors have given approval to the final version of the manuscript.

Data Availability Statement

The data that support the findings of this study are available from the corresponding author upon reasonable request.

Keywords

breaking scaling relationship, density functional theory (DFT) calculations, dual-atom catalysts, electrocatalytic CO₂ reduction, electron interaction

Received: October 13, 2023

Published online:

- [1] M. B. Ross, P. De Luna, Y. Li, C.-T. Dinh, D. Kim, P. Yang, E. H. Sargent, *Nat. Catal.* **2019**, *2*, 648.
- [2] C. Xu, X. Zhi, A. Vasileff, D. Wang, B. Jin, Y. Jiao, Y. Zheng, S.-Z. Qiao, *Small Struct.* **2020**, *2*, 2000058.
- [3] Y. Zhu, X. Yang, C. Peng, C. Priest, Y. Mei, G. Wu, *Small* **2021**, *17*, e2005148.
- [4] S. Wei, Y. Wang, W. Chen, Z. Li, W.-C. Cheong, Q. Zhang, Y. Gong, L. Gu, C. Chen, D. Wang, Q. Peng, Y. Li, *Chem. Sci.* **2019**, *11*, 786.
- [5] M. G. Kibria, J. P. Edwards, C. M. Gabardo, C.-T. Dinh, A. Seifitokaldani, D. Sinton, E. H. Sargent, *Adv. Mater.* **2019**, *31*, 1807166.
- [6] W. Zhou, K. Cheng, J. Kang, C. Zhou, V. Subramanian, Q. Zhang, Y. Wang, *Chem. Soc. Rev.* **2019**, *48*, 3193.
- [7] M. D. Porosoff, J. G. Chen, *J. Catal.* **2013**, *301*, 30.
- [8] Q. Sun, C. Jia, Y. Zhao, C. Zhao, *Chinese J. Catal.* **2022**, *43*, 1547.
- [9] C. Chen, J. F. Khosrowabadi Kotyk, S. W. Sheehan, *Chem.-Us* **2018**, *4*, 2571.
- [10] X. Tan, X. Sun, B. Han, *Natl. Sci. Rev.* **2022**, *9*, nwab022.
- [11] S. Ji, Y. Chen, X. Wang, Z. Zhang, D. Wang, Y. Li, *Chem. Rev.* **2020**, *120*, 11900.
- [12] Y. Zhao, Z. Pei, X. F. Lu, D. Luan, X. Wang, X. W. (D.) Lou, *Chem. Catalysis* **2022**, *2*, 1480.
- [13] Y. Pan, R. Lin, Y. Chen, S. Liu, W. Zhu, X. Cao, W. Chen, K. Wu, W.-C. Cheong, Y. Wang, L. Zheng, J. Luo, Y. Lin, Y. Liu, C. Liu, J. Li, Q. Lu, X. Chen, D. Wang, Q. Peng, C. Chen, Y. Li, *J. Am. Chem. Soc.* **2018**, *140*, 4218.
- [14] K. Jiang, S. Siahrostami, T. Zheng, Y. Hu, S. Hwang, E. Stavitski, Y. Peng, J. Dynes, M. Gangisetty, D. Su, K. Attenkofer, H. Wang, *Energ. Environ. Sci.* **2018**, *11*, 893.
- [15] W. Guo, X. Tan, J. Bi, L. Xu, D. Yang, C. Chen, Q. Zhu, J. Ma, A. Tayal, J. Ma, Y. Huang, X. Sun, S. Liu, B. Han, *J. Am. Chem. Soc.* **2021**, *143*, 6877.
- [16] B. Qiao, A. Wang, X. Yang, L. F. Allard, Z. Jiang, Y. Cui, J. Liu, J. Li, T. Zhang, *Nat. Chem.* **2011**, *3*, 634.
- [17] W. Ju, A. Bagger, G.-P. Hao, A. S. Varela, I. Sinev, V. Bon, B. Roldan Cuenya, S. Kaskel, J. Rossmeisl, P. Strasser, *Nat. Commun.* **2017**, *8*, 944.
- [18] F. Yang, P. Song, X. Liu, B. Mei, W. Xing, Z. Jiang, L. Gu, W. Xu, *Angew. Chem., Int. Ed.* **2018**, *130*, 12483.
- [19] T. Zheng, K. Jiang, N. Ta, Y. Hu, J. Zeng, J. Liu, H. Wang, *Joule* **2019**, *3*, 265.
- [20] X. Wang, Z. Chen, X. Zhao, T. Yao, W. Chen, R. You, C. Zhao, G. Wu, J. Wang, W. Huang, J. Yang, X. Hong, S. Wei, Y. Wu, Y. Li, *Angew. Chem., Int. Ed.* **2018**, *57*, 1944.
- [21] W. Ren, X. Tan, W. Yang, C. Jia, S. Xu, K. Wang, S. C. Smith, C. Zhao, *Angew. Chem., Int. Ed.* **2019**, *58*, 6972.
- [22] W. Xie, H. Li, G. Cui, J. Li, Y. Song, S. Li, X. Zhang, J. Y. Lee, M. Shao, M. Wei, *Angew. Chem., Int. Ed.* **2021**, *60*, 7382.

- [23] S.-G. Han, D.-D. Ma, S.-H. Zhou, K. Zhang, W.-B. Wei, Y. Du, X.-T. Wu, Q. Xu, R. Zou, Q.-L. Zhu, *Appl. Catal. B: Environ.* **2021**, 283, 119591.
- [24] H. Zhang, J. Li, S. Xi, Y. Du, X. Hai, J. Wang, H. Xu, G. Wu, J. Zhang, J. Lu, J. Wang, *Angew. Chem., Int. Ed.* **2019**, 58, 14871.
- [25] A. S. Varela, N. Ranjbar Sahraie, J. Steinberg, W. Ju, H.-S. Oh, P. Strasser, *Angew. Chem., Int. Ed.* **2015**, 54, 10758.
- [26] K. Li, S. Zhang, X. Zhang, S. Liu, H. Jiang, T. Jiang, C. Shen, Y. Yu, W. Chen, *Nano Lett.* **2022**, 22, 1557.
- [27] F. Pan, B. Li, E. Sarnello, Y. Fei, X. Feng, Y. Gang, X. Xiang, L. Fang, T. Li, Y. H. Hu, G. Wang, Y. Li, *ACS Catal.* **2020**, 10, 10803.
- [28] S. Chen, X. Li, C.-W. Kao, T. Luo, K. Chen, J. Fu, C. Ma, H. Li, M. Li, T.-S. Chan, M. Liu, *Angew. Chem., Int. Ed.* **2022**, 61, 202206233.
- [29] W. Zhu, L. Zhang, S. Liu, A. Li, X. Yuan, C. Hu, G. Zhang, W. Deng, K. Zang, J. Luo, Y. Zhu, M. Gu, Z. Zhao, J. Gong, *Angew. Chem., Int. Ed.* **2020**, 59, 12664.
- [30] J.-D. Yi, X. Gao, H. Zhou, W. Chen, Y. Wu, *Angew. Chem., Int. Ed.* **2022**, 61, 202212329.
- [31] H. Cheng, X. Wu, M. Feng, X. Li, G. Lei, Z. Fan, D. Pan, F. Cui, G. He, *ACS Catal.* **2021**, 11, 12673.
- [32] Y. Li, B. Wei, M. Zhu, J. Chen, Q. Jiang, B. Yang, Y. Hou, L. Lei, Z. Li, R. Zhang, Y. Lu, *Adv. Mater.* **2021**, 33, 2102212.
- [33] Y. Li, W. Shan, M. J. Zachman, M. Wang, S. Hwang, H. Tabassum, J. Yang, X. Yang, S. Karakalos, Z. Feng, G. Wang, G. Wu, *Angew. Chem., Int. Ed.* **2022**, 61, 202205632.
- [34] W. Cheng, X. F. Lu, D. Luan, X. W. (D.). Lou, *Angew. Chem., Int. Ed.* **2020**, 59, 18234.
- [35] Q. Hao, H.-X. Zhong, J.-Z. Wang, K.-H. Liu, J.-M. Yan, Z.-H. Ren, N. Zhou, X. Zhao, H. Zhang, D.-X. Liu, X. Liu, L.-W. Chen, J. Luo, X.-B. Zhang, *Nat. Synth.* **2022**, 1, 719.
- [36] B. Zhang, J. Zhang, J. Shi, D. Tan, L. Liu, F. Zhang, C. Lu, Z. Su, X. Tan, X. Cheng, B. Han, L. Zheng, J. Zhang, *Nat. Commun.* **2019**, 10, 2980.
- [37] S. Lu, Y. Zhang, M. F. Mady, O. Egwu Eleri, W. Mekonnen Tucho, M. Mazur, A. Li, F. Lou, M. Gu, Z. Yu, *ChemSusChem* **2022**, 15, 202200870.
- [38] J. Leverett, T. Tran-Phu, J. A. Yuwono, P. Kumar, C. Kim, Q. Zhai, C. Han, J. Qu, J. Cairney, A. N. Simonov, R. K. Hocking, L. Dai, R. Daiyan, R. Amal, *Adv. Energy Mater.* **2022**, 12, 2201500.
- [39] Y. Zheng, Y. Jiao, L. Ge, M. Jaroniec, S. Z. Qiao, *Angew. Chem., Int. Ed.* **2013**, 52, 3110.
- [40] W. Dong, N. Zhang, S. Li, S. Min, J. Peng, W. Liu, D. Zhan, H. Bai, *J. Mater. Chem. A* **2022**, 10, 10892.
- [41] D. Yao, C. Tang, X. Zhi, B. Johannessen, A. Slattery, S. Chern, S.-Z. Qiao, *Adv. Mater.* **2023**, 35, 2209386.
- [42] Z. Lu, J. Wang, S. Huang, Y. Hou, Y. Li, Y. Zhao, S. Mu, J. Zhang, Y. Zhao, *Nano Energy* **2017**, 42, 334.
- [43] X. Li, X. Huang, S. Xi, S. Miao, J. Ding, W. Cai, S. Liu, X. Yang, H. Yang, J. Gao, J. Wang, Y. Huang, T. Zhang, B. Liu, *J. Am. Chem. Soc.* **2018**, 140, 12469.
- [44] H. Cheng, X. Wu, X. Li, Y. Zhang, M. Feng, Z. Fan, G. He, *J. Catal.* **2021**, 395, 63.
- [45] H. Chen, X. Guo, X. Kong, Y. Xing, Y. Liu, B. Yu, Q.-X. Li, Z. Geng, R. Si, J. Zeng, *Green Chem.* **2020**, 22, 7529.
- [46] H. Yang, P. Zhang, X. Yi, C. Yan, D. Pang, L. Chen, S. Wang, C. Wang, B. Liu, G. Zhang, Z. Zhou, X. Li, *Chem. Eng. J.* **2022**, 440, 135749.
- [47] Z. Li, R. Wu, S. Xiao, Y. Yang, L. Lai, J. S. Chen, Y. Chen, *Chem. Eng. J.* **2022**, 430, 132882.
- [48] F. Pan, B. Li, W. Deng, Z. Du, Y. Gang, G. Wang, Y. Li, *Appl. Catal. B: Environ.* **2019**, 252, 240.
- [49] J. Feng, H. Gao, L. Zheng, Z. Chen, S. Zeng, C. Jiang, H. Dong, L. Liu, S. Zhang, X. Zhang, *Nat. Commun.* **2020**, 11, 4341.
- [50] J. Yang, Z. Qiu, C. Zhao, W. Wei, W. Chen, Z. Li, Y. Qu, J. Dong, J. Luo, Z. Li, Y. I. Wu, *Angew. Chem., Int. Ed.* **2018**, 57, 14095.
- [51] Y.-N. Gong, L. Jiao, Y. Qian, C.-Y. Pan, L. Zheng, X. Cai, B. Liu, S.-H. Yu, H.-L. Jiang, *Angew. Chem., Int. Ed.* **2020**, 59, 2705.
- [52] R. Yun, F. Zhan, X. Wang, B. Zhang, T. Sheng, Z. Xin, J. Mao, S. Liu, B. Zheng, *Small* **2021**, 17, 2006951.
- [53] H. Yang, Q. Lin, C. Zhang, X. Yu, Z. Cheng, G. Li, Q. Hu, X. Ren, Q. Zhang, J. Liu, C. He, *Nat. Commun.* **2020**, 11, 593.
- [54] M. Ma, B. J. Trzesniewski, J. Xie, W. A. Smith, *Angew. Chem., Int. Ed.* **2016**, 55, 9748.
- [55] N. Zhang, X. Zhang, L. Tao, P. Jiang, C. Ye, R. Lin, Z. Huang, A. Li, D. Pang, H. Yan, Y. Wang, P. Xu, S. An, Q. Zhang, L. Liu, S. Du, X. Han, D. Wang, Y. Li, *Angew. Chem., Int. Ed.* **2021**, 60, 6170.